

## Differential-frequency Doppler weather radar: Theory and experiment

R. Meneghini, S. W. Bidwell, R. Rincon, and G. M. Heymsfield

National Aeronautics and Space Administration/Goddard Space Flight Center, Greenbelt, Maryland, USA

L. Liao

Caelum Research Corp., Rockville, Maryland, USA

Received 6 March 2002; revised 10 July 2002; accepted 21 August 2002; published 7 February 2003.

[1] To move toward spaceborne weather radars that can be deployed routinely as part of an instrument set consisting of passive and active sensors requires the development of smaller, lighter-weight radars. At the same time, the addition of a second frequency and an upgrade to Doppler capability are essential to retrieve information on the drop size distribution (DSD), vertical air motion, and storm dynamics. One approach to the problem is to use a single broadband transmitter-receiver and antenna where two narrowband frequencies are spaced apart by 7–10%. Use of Ka-band frequencies (26.5–40 GHz) provides adequate spatial resolution with a relatively small antenna. Moreover, the differential reflectivity and mean Doppler signals in this band are directly related to the median mass diameter of the snow and raindrop size distributions. We present in the paper theoretical calculations of the differential reflectivity and Doppler for several frequency pairs including those proposed for the Global Precipitation Mission (GPM) at 13.6 and 35 GHz. Measurements from a zenith-directed radar operated at 9.1 and 10 GHz are used to investigate the qualitative characteristics of the differential signals. Disdrometer data taken at the surface, just below the radar, show that the differential signals are related to characteristics of the raindrop size distribution. The stability of the DSD estimation procedure is tested using a simulation. The results indicate that reasonably stable estimates of the particle size distribution are feasible with a [31.5 GHz, 35 GHz] combination as long as a large number of independent samples are obtained. *INDEX TERMS*: 0360 Atmospheric Composition and Structure: Transmission and scattering of radiation; 0629 Electromagnetics: Inverse scattering; 0694 Electromagnetics: Instrumentation and techniques; 1854 Hydrology: Precipitation (3354); 3360 Meteorology and Atmospheric Dynamics: Remote sensing; *KEYWORDS*: Doppler, radar, differential-frequency, rain, spaceborne radar, drop size distribution

**Citation:** Meneghini, R., S. W. Bidwell, R. Rincon, G. M. Heymsfield, and L. Liao, Differential-frequency Doppler weather radar: Theory and experiment, *Radio Sci.*, 38(3), 8040, doi:10.1029/2002RS002656, 2003.

### 1. Introduction and Background

[2] The Precipitation Radar (PR) aboard the Tropical Rain Measuring Mission (TRMM) satellite has performed nearly flawlessly since its launch in December 1997 [Kozu *et al.*, 2001]. The PR is the first weather radar to be flown in space and the question arises as to the design of the next-generation weather radar. This question has been answered, in part, by the proposed radar for the successor to TRMM, the Global Precipitation Mission

(GPM). The tentative plan for the GPM radar is to employ dual-frequencies at 13.6 GHz and 35 GHz, with phased-array antennas that scan cross-track with beam widths matched at the two frequencies. This dual-frequency precipitation radar, DPR, should provide more detailed information on the drop size distribution and phase state of the hydrometeors (liquid, frozen, and mixed-phase) than does the present single-frequency 13.8 GHz PR. The DPR should also provide an increase in the dynamic range of observable rain rates and better accuracy in the estimates of rain rate and liquid and ice water contents. In this paper we focus on an alternative design strategy that makes use of the differential-frequency concept. The

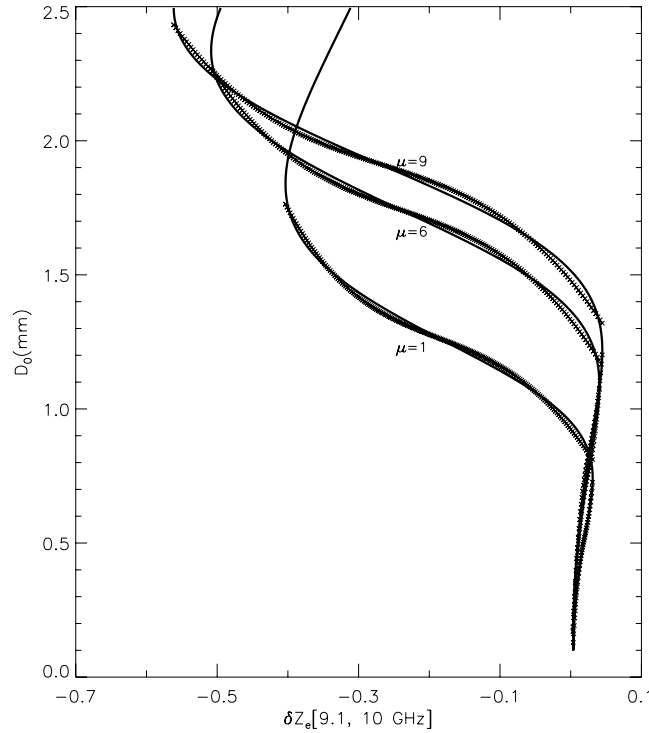


**Figure 1.**  $D_0$  versus  $\delta Z_e[9.1, 10 \text{ GHz}]$  for 3 values of  $\mu$  along with cubic fits to the lower and upper branches (X).

essence of the idea is to reduce the spacing between the two frequencies so that a single antenna and the same radio-frequency subsystem can be used for both frequencies. The resulting reduction in size and mass suggests the possibility of weather radars aboard smaller satellites or as an add-on instrument to weather-related satellites that are presently equipped with only passive radiometers.

[3] We begin by presenting theoretical calculations of the differential reflectivity and mean Doppler for several differential frequency combinations. These results are then compared with the same quantities using the DPR frequencies of 13.6 and 35 GHz. We next present results measured from a ground-based zenith-looking radar operating at [9.1, 10 GHz]. Raindrop size distributions from a disdrometer located near the radar are used to estimate the expected differential signals to check the validity of the theory and to test whether differential signals can be measured down to X-band frequencies. In the final section, we present integral equations that offer a means of retrieving two parameters of the drop size distribution at each range gate along the radar beam. Using these equations and measured drop size distributions as truth, simulations are carried out for several frequency pairs including those of the DPR. The simulations suggest that frequencies at Ka-band using a 10% bandwidth can give useful information on the raindrop size distribution if a sufficient number of independent samples can be measured.

## 2. Theoretical Calculations

[4] We define the differential-frequency radar reflectivity,  $\delta Z_e(f_1, f_2)$ , by [Meneghini *et al.*, 2001]

$$\delta Z_e(f_1, f_2) = \text{dB}Z_e(f_1) - \text{dB}Z_e(f_2) \quad (1)$$

where  $f_1 < f_2$  so that  $\delta Z_e$  is always taken as the difference between  $\text{dB}Z_e$  at the lower frequency to that at the higher frequency. The equivalent reflectivity factor at frequency  $f$  is given by  $\text{dB}Z_e(f) = 10 \log_{10} Z_e(f)$  where

$$Z_e(f) = c^4 / [f^4 \pi^5 |K_w|^2] \int \sigma_b(f, D) N(D) dD \quad (2)$$

where  $c$  is the speed of light,  $\sigma_b(f, D)$  is the back-scattering cross section ( $\text{mm}^2$ ) of a spherical particle of diameter  $D$  at frequency  $f$  and  $N(D)$  is the drop size distribution, DSD, ( $\text{mm}^{-1} \text{m}^{-3}$ ). Taking the units of  $\lambda = c/f$  and  $dD$  to be mm gives the equivalent reflectivity factor in the standard units of  $\text{mm}^6 \text{m}^{-3}$ . By convention, the dielectric factor of water,  $|K_w|^2$ , is taken to be 0.93. We assume that  $N(D)$  can be approximated by a gamma distribution [Ulbrich, 1983]

$$N(D) = N_0 D^\mu \exp[-(3.67 + \mu)D/D_0] \quad (3)$$

The unknown parameters of the size distribution are  $(N_0, D_0, \mu)$ . Dual-wavelength radar data provide only two

measurements at each range gate. To account for the third unknown, the “shape” parameter  $\mu$  is either fixed or a  $\mu$ - $\Lambda$  (where  $\Lambda D_0 = 3.67 + \mu$ ) relationship is employed [Zhang *et al.*, 2001]. We can define a differential mean Doppler velocity,  $\delta v$ , in a similar way to  $\delta Z_e$ :

$$\delta v(f_1, f_2) = \langle v(f_1) \rangle - \langle v(f_2) \rangle \quad (4)$$

where  $\delta v(f_1, f_2)$  is independent of air motion or platform motion. In the absence of air or platform motion, the Doppler velocity for a near-zenith or near-nadir, narrow beam pattern can be written as a function of the terminal velocity of the drops,  $v_t$ , weighted by  $\sigma_b(f, D) N(D)$  [Atlas, 1964; Doviak and Zrnice, 1993]:

$$\langle v(f) \rangle = \int_D \sigma_b(f, D) N(D) v_t(D) dD / \int_D \sigma_b(f, D) N(D) dD \quad (5)$$

[5] Shown in Figure 1 are graphs  $D_0$  versus  $\delta Z_e$  for the frequency pair [9.1, 10 GHz] for values of  $\mu = 1, 6$ , and 9. Note that  $\delta Z_e$  is independent of the  $N_0$  parameter of the size distribution. The temperature of the raindrops is taken to be 20 C. As expected, as the median mass diameter decreases, Rayleigh scattering predominates. In this limit the  $Z_e$  at both frequencies is equal to the sixth moment of the drop size distribution so that  $\delta Z_e$  tends to zero for small  $D_0$ . Also shown in the figure are the results of cubic fits to the “upper” and “lower” branches of the form  $D_0 = c_0 + c_1 \delta Z_e + c_2 (\delta Z_e)^2 + c_3 (\delta Z_e)^3$ , and represented by the X’s. These curve-fits alone do not provide a  $D_0$  estimate, however, unless we know which branch to select. Moreover, for  $\mu = 1$ , the estimation of  $D_0$  from  $\delta Z_e$  is ambiguous not only for  $\delta Z_e > 0$  but for  $\delta Z_e < -0.3$  dB as well and an additional selection rule is needed. One other problem is that the magnitude of  $\delta Z_e$  is less than 0.6 dB over the full range of  $D_0$  which implies that a large number of independent samples are needed for the differential signal to be distinguishable from inherent fluctuations in the measurement. These issues will be taken up in section 4. It is worth noting that in snow the ambiguity of estimating  $D_0$  from  $\delta Z_e$  is absent because  $D_0$  is a monotonically increasing function of  $\delta Z_e$  for all frequency pairs in the microwave and millimeter-wave range [Matrosov, 1992; Meneghini *et al.*, 1992].

[6] It is instructive to compare curves of  $D_0$  versus  $\delta Z_e$  for other frequency combinations. Such plots are shown in the top panel of Figure 2 for the DPR frequencies of [13.6, 35 GHz] and in the bottom panel for the [31.5, 35 GHz] pair. In contrast to the [9.1, 10 GHz] curves,  $\delta Z_e$  for these cases is negative at small  $D_0$  changing to positive values at larger  $D_0$ . From Figure 1, we see that the magnitude of  $\delta Z_e$ [9.1, 10 GHz] is typically about a factor of 3 smaller than  $\delta Z_e$ [31.5, 35 GHz] and about an order of magnitude smaller than  $\delta Z_e$ [13.6, 35 GHz]. Although the DPR fre-

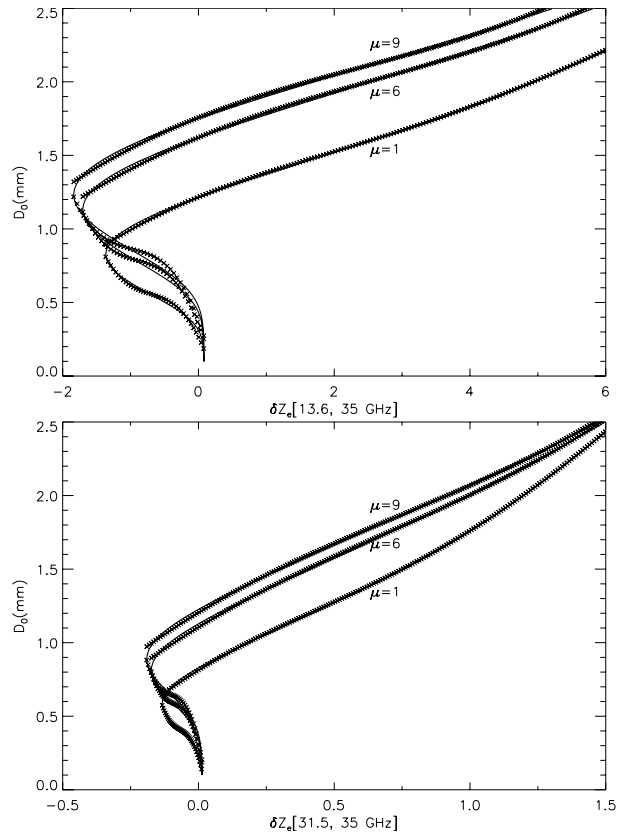


**Figure 2.** Same as bottom plot of Figure 1 but for the frequency pairs (13.6, 35 GHz) top and (31.5, 35 GHz) bottom.  $T = 20$  C.

quency pair provides a larger differential reflectivity signal than that at [31.5, 35 GHz], the ambiguity problem is more severe. In the case of  $\mu = 6$ , for example, the estimate of  $D_0$  from  $\delta Z_e$ [13.6, 35 GHz] is ambiguous for  $D_0$  less than 1.63 mm whereas two solutions of  $D_0$  exist for the [31.5, 35 GHz] combination when  $D_0$  less than 1.14 mm.

[7] Similar sets of plots can be generated for  $D_0$  versus  $\delta v$ . These are shown in Figure 3 for the frequency pairs [9.1, 10 GHz] (top) and [13.6, 35 GHz] (bottom). For the [9.1, 10 GHz] combination cubic fits of  $D_0$  versus  $\delta v$  for the lower and upper branches are represented by the “X” data points. As can be seen from the results, the  $|\delta v$ [9.1, 10 GHz]| values, ranging from 0 to about 10 cm/s, are about an order of magnitude smaller than  $|\delta v$ [13.6, 35 GHz]| and about 2 orders of magnitude smaller than typical mean Doppler velocities.

### 3. Experimental Data

[8] Differential frequency measurements were made using the ER-2 Doppler radar (EDOP) in a ground-

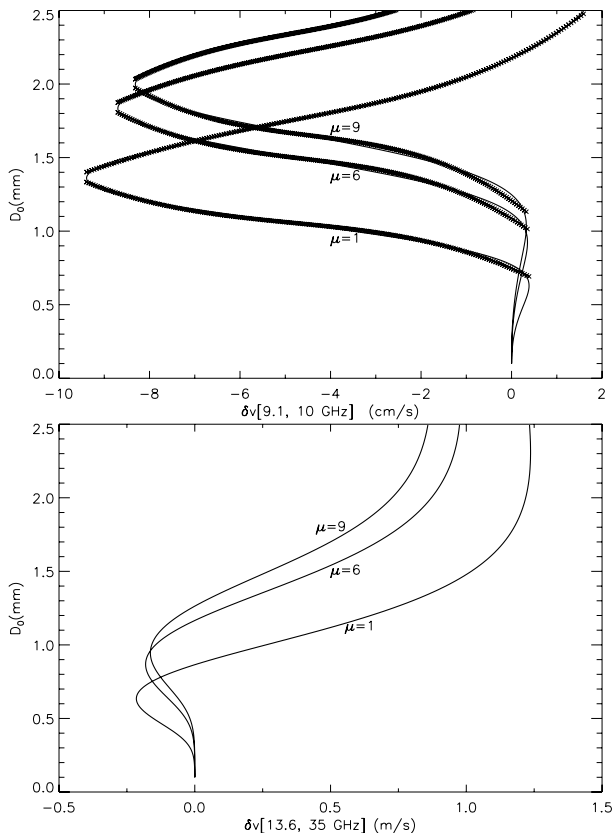


**Figure 3.** Top:  $D_0$  versus  $\delta v[9.1, 10 \text{ GHz}]$  for 3 values of  $\mu$  along with cubic fits to the lower and upper branches. Bottom:  $D_0$  versus  $\delta v[13.6, 35 \text{ GHz}]$  for 3 values of  $\mu$ .  $T = 20 \text{ C}$ .

based, zenith-looking configuration [Heymsfield *et al.*, 1996]. To modify the EDOP for differential measurements, the local oscillator (LO) at 9.6 GHz was disconnected and replaced with two synthesized HP-83640 sweep generators. These oscillators were used both to generate the transmit pulse and to mix the received signals down to the intermediate frequency (IF). The LO frequencies were chosen to produce transmit frequencies of 9.1 and 10 GHz, a separation that was found to be the practical limit based on the performance characteristics of the EDOP traveling wave tube amplifier (TWTA). Generation, transmission, and reception of the two frequencies were done simultaneously [Bidwell *et al.*, 2000].

[9] On 27 March 2000, an impact disdrometer and optical rain gauge were placed next to the zenith-directed antenna. Approximately 3 hours of data were collected. Because the modified radar was uncalibrated, the radar return powers were converted into radar reflectivities by

additive constants (one per frequency) using the drop size distribution data near the beginning of the measurement period. Height versus time plots of  $Z_{me}(9.1 \text{ GHz})$  and  $\delta Z_{me}[9.1, 10 \text{ GHz}]$  are shown in the top and center panels of Figure 4. (As discussed in section 4, the subscript “m” is used to signify the fact that the radar reflectivity factors are measured quantities, without attenuation correction.) Note that the  $Z_{me}(9.1 \text{ GHz})$  data extend to higher altitudes than do the  $\delta Z_{me}[9.1, 10 \text{ GHz}]$  data; this arises from the facts that  $\delta Z_{me}[9.1, 10 \text{ GHz}]$  is calculated only when both radar reflectivities are above the noise level and that the sensitivity of the  $Z_{me}(10 \text{ GHz})$  data set is lower than that at  $Z_{me}(9.1 \text{ GHz})$ . Displayed in the bottom panel are selected vertical profiles of  $\delta Z_{me}$ . Corresponding plots of  $\langle v(9.1 \text{ GHz}) \rangle$  and  $\delta v[9.1, 10 \text{ GHz}]$  are shown in Figure 5. Although the data in Figures 4 and 5 include a convective cell, the rain on this day was primarily stratiform with a bright-band (melting layer) signature at a height of about 2.2 km. To

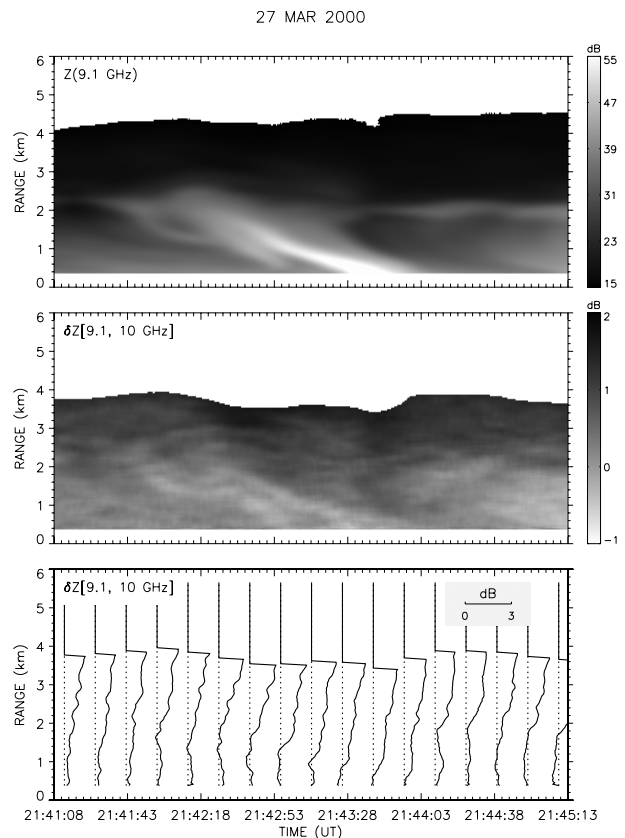


**Figure 4.** Height versus time plots of  $Z_{me}(9.1 \text{ GHz})$  (top),  $\delta Z_{me}[9.1, 10 \text{ GHz}]$  (center) and height profiles of  $\delta Z_{me}[9.1, 10 \text{ GHz}]$  (bottom) over a 4 min segment of data. See color version of this figure at back of this issue.

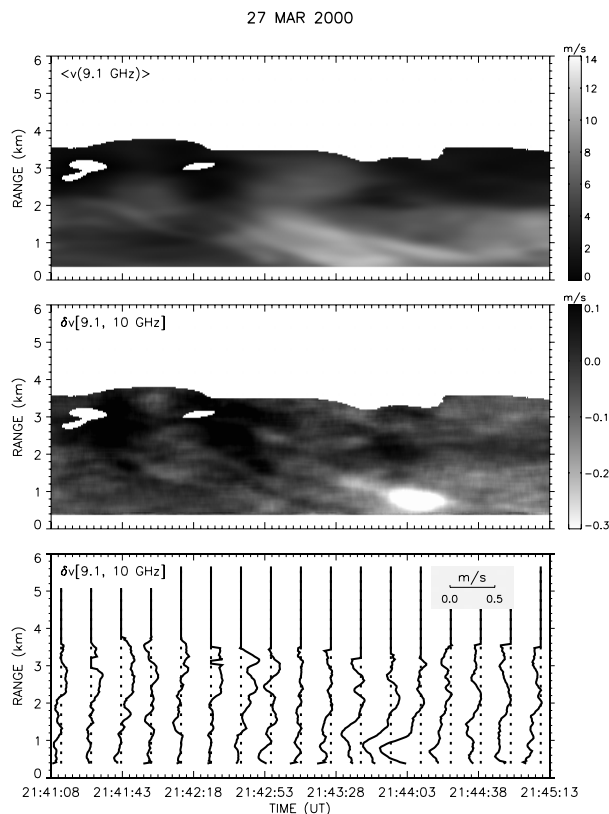


**Figure 5.** Height versus time plots of the mean Doppler velocity,  $\langle v(9.1 \text{ GHz}) \rangle$  (top),  $\delta v[9.1, 10 \text{ GHz}]$  (center) and height profiles of  $\delta v[9.1, 10 \text{ GHz}]$  (bottom) over same 4 min segment of data as in Figure 4. See color version of this figure at back of this issue.

understand the behavior of  $\delta Z_{me}$  at X-band frequencies recall that in rain,  $\delta Z_e$  is negative for most  $D_0$  values (see Figure 1) with larger  $D_0$  values usually associated with larger values of  $|\delta Z_e|$ . As the signals propagate into the rain the measured differential reflectivity,  $\delta Z_{me}$ , becomes progressively less negative because attenuation at the higher frequency is larger than that at the lower. In dry snow,  $\delta Z_e$  is always positive so that a change of sign of  $\delta Z_{me}$  occurs as the signal transits the melting layer.

[10] Somewhat similar characteristics can be seen in the differential mean Doppler results pictured in the center and lower panels of Figure 5. In contrast to  $\delta Z_{me}$ ,  $\delta v$  is insensitive to differential attenuation. Moreover, a comparison of the theoretical curves in Figures 1 and 3 shows that the dependencies of  $\delta Z_e$  and  $\delta v$  on  $D_0$  differ, particularly at large  $D_0$ . In the snow layer,  $\delta v$  is approximately zero whereas  $\delta Z_e$  attains relatively large positive values.

[11] To test the measurement concept, it is important to show the relation between the differential signals and the drop size distributions. To do this, we have used the disdrometer data and Mie theory to calculate the expected values of  $Z_e$ ,  $\delta Z_e$ ,  $\langle v \rangle$  and  $\delta v$ . An example of comparisons between the disdrometer-derived  $Z_e$  (top panel) and  $\delta Z_e$  (bottom panel) and the corresponding EDOP measurements is shown in Figure 6. A 60-s shift of the EDOP data was introduced to account for the fact that the EDOP data were taken at a 400m height. Because the data analyzed are taken near the radar, the attenuation can be neglected so that  $\delta Z_e = \delta Z_{me}$  and  $Z_e = Z_{me}$ . A second set of comparisons is shown in Figure 7 where the top plot shows a time sequence of measured  $\langle v(9.1 \text{ GHz}) \rangle$  (X) along with the disdrometer-derived values (solid line). In the lower panel of Figure 7 are shown measurements of  $\delta v$  (X) values along with the disdrometer-derived values (solid line). Although the EDOP estimates of  $\delta Z_e$  are noisy, the correlation between these and DSD-derived estimates is relatively good. This is encouraging in the sense that the [9.1, 10 GHz] combination is far from optimum, suggesting that sets of frequencies at Ka-band, separated by 7% to 10%, should yield more stable estimates of  $\delta Z_e$ . On the other hand, comparisons between the theoretical and experimental values of  $\delta v$  in Figure 7, while showing some degree of correlation, are poor and radar data at higher frequencies with a greater frequency separation may be required to demonstrate the correspondence between theory and experimental data.

#### 4. DSD Estimation Using Differential Frequencies

[12] The EDOP measurements discussed in the previous section indicate that measurements of  $\delta Z_e$  and  $\delta v$  are possible at X-band and that  $\delta Z_e$ , and to a lesser extent  $\delta v$ , are associated with properties of the raindrop size distribution. Nevertheless, as noted in section 2, there are a number of issues that must be addressed before we can show the feasibility of measuring vertical profiles of the drop size distribution, rain rate and liquid water content. The chief problems include the double-valued nature of the  $D_0$  versus  $\delta Z_e$  (and  $D_0$  versus  $\delta v$ ) curves for rain and the fact that the parameter  $\mu$  of the drop size distribution can not be solved directly but must be either fixed or related to the parameter  $D_0$  or  $\Lambda$ . Moreover, the differential signal levels are small, requiring a large number of independent samples to reduce the signal fluctuations to an acceptable level. One other problem associated with  $\delta Z_e$ , though not with  $\delta v$ , is the influence of attenuation. According to (1),  $\delta Z_e$  is a difference in dB of the effective radar reflectivity factors,  $Z_e(f_1)$  and  $Z_e(f_2)$ . But it is the apparent or measured radar reflectivity,

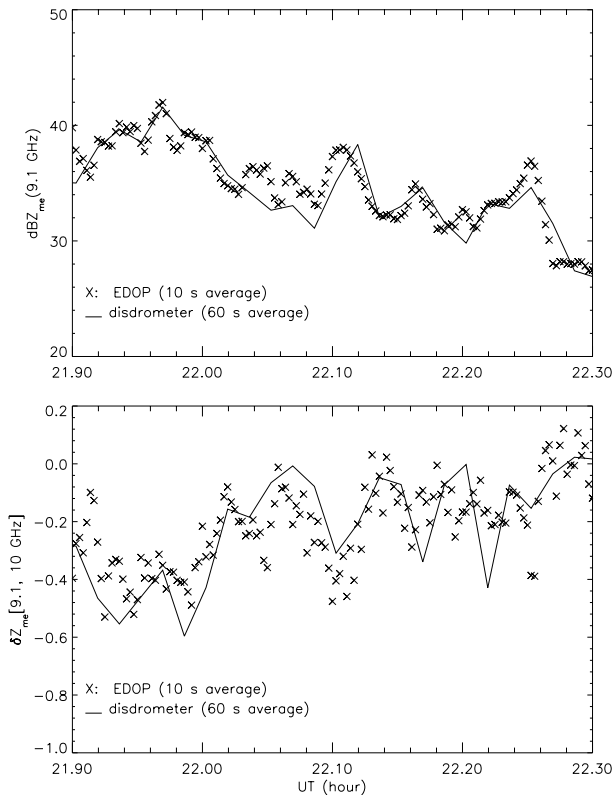


**Figure 6.** Comparisons of EDOP measurements (X) and disdrometer-derived (solid lines) values of  $Z_{me}(9.1 \text{ GHz})$  (top) and  $\delta Z_{me}[9.1, 10 \text{ GHz}]$  (bottom).

$Z_{me}(f)$ , and not  $Z_e(f)$ , that is directly related to the radar return power. In particular,  $Z_{me}(f)$  and  $Z_e(f)$  are related by:

$$Z_{me}(f, r) = Z_e(f, r) \exp \left[ -0.2 \ln 10 \int_0^r k(f, s) ds \right] \quad (6)$$

where  $r$  is the radar range. The specific attenuation,  $k$  (dB/km), can be written in the form:

$$k(f) = N_0 I_e(f, D_0) \quad (7)$$

where  $I_e(f, D_0)$  is a function of the extinction cross section,  $\sigma_e(f, D)$  ( $\text{mm}^2$ ) integrated over the “normalized” DSD—that is, the DSD without the  $N_0$  coefficient:

$$I_e(f, D_0) = c_k \int \sigma_e(f, D) D^\mu \exp[-(3.67 + \mu)D/D_0] dD \quad (8)$$

where  $c_k = 4.343 \times 10^{-3}$ . Integral or differential equations for the DSD parameters  $N_0(r)$  and  $D_0(r)$  can be derived in several ways [Meneghini *et al.*, 1992; Iguchi and Meneghini, 1995]. A particularly simple way to obtain them is to express  $10 \log_{10}\{Z(f_1, r)/Z(f_2, r)\}$  and  $10 \log_{10}[Z(f_1, r)]$  in terms of parameters of DSD and the measured reflectivity factors. To simplify the equations, we introduce the following notation:

$$I_b(f, D_0) = 10 \log_{10} Z_e(f, D_0, N_0) - 10 \log_{10} N_0 \quad (9)$$

$$= 10 \log_{10} \left\{ c^4 / \left[ f^4 \pi^5 |K_w|^2 \right] \right.$$

$$\left. \cdot \int \sigma_b(f, D) D^\mu \exp[-(3.67 + \mu)D/D_0] dD \right\} \quad (10)$$

[13] The initial-value equations can be written in the form:

$$\delta I_b[f, D_0(r)] = \delta Z_{me}(f, r) + 2 \int_0^r N_0(s) \delta I_e[f, D_0(s)] ds \quad (11a)$$

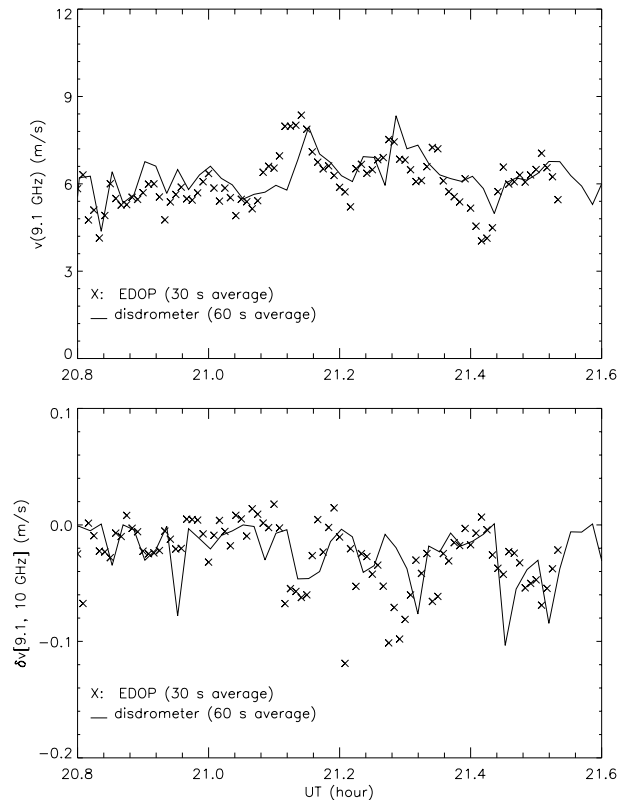


**Figure 7.** Comparisons of EDOP measurements (X) and disdrometer-derived (solid lines) values of  $\langle v(9.1 \text{ GHz}) \rangle$  (top) and  $\delta v[9.1, 10 \text{ GHz}]$  (bottom).

$$\begin{aligned} \text{dB}N_0(r) &= \text{dB}Z_{\text{me}}(f_1, r) - I_b[f_1, D_0(r)] + 2 \\ &\cdot \int_0^r N_0(s) I_c[f_1, D_0(s)] ds \end{aligned} \quad (11b)$$

where  $\text{dB}N_0 = 10 \log_{10} N_0$ . A final-value form of the equations is appropriate to cases where independent estimates of the path-integrated attenuation, PIA, are available at both frequencies. In this case, the equations can be written:

$$\begin{aligned} \delta I_b[f, D_0(r)] &= \delta Z_{\text{me}}(f, r) + 2 \delta A_n(f) - 2 \\ &\cdot \int_r^{r_n} N_0(s) \delta I_c[f, D_0(s)] ds \end{aligned} \quad (12a)$$

$$\begin{aligned} \text{dB}N_0(r) &= \text{dB}Z_{\text{me}}(f_1, r) - I_b[f_1, D_0(r)] + 2 A_n(f_1) - 2 \\ &\cdot \int_r^{r_n} N_0(s) I_c[f, D_0(s)] ds \end{aligned} \quad (12b)$$

where  $\delta I_b = I_b(f_1) - I_b(f_2)$ ,  $\delta I_c = I_c(f_1) - I_c(f_2)$  and where  $\delta Z_{\text{me}}(f, r) \equiv 10 \log_{10} Z_{\text{me}}(f_1, r) - 10 \log_{10} Z_{\text{me}}(f_2, r)$ . In all cases,  $f_1 < f_2$ . Note that  $A_n(f_1)$  is an independent estimate of the PIA at frequency  $f_1$  and  $\delta A_n(f)$  is an independent estimate of the differential PIA. Defining the path to run from radar range 0 to  $r_n$ , these quantities can be written in the form:

$$A_n(f_1) = \int_0^{r_n} k(f_1, s) ds \quad (13)$$

$$\delta A_n(f) = \int_0^{r_n} [k(f_1, s) - k(f_2, s)] ds \quad (14)$$

Equations (11a), (11b), (12a), and (12b) are coupled Volterra integral equations for the unknown parameters of the drop size distributions  $N_0(r)$  and  $D_0(r)$  ( $0 < r < r_n$ ) in terms of the measured quantities  $\delta Z_{\text{me}}(f, r)$  and  $\text{dB}Z_{\text{me}}(f_1, r)$ . For the final value equations (12a) and (12b), we also require the path-integrated quantities  $\delta A_n(f)$  and  $A_n(f_1)$ . The physical meaning of the equations becomes clear by recognizing that  $\delta I_b[f, D_0(r)] = \delta Z_c[f, D_0(r)]$  and that (11a) and (12a) are of the form  $\delta Z_c = \delta Z_{\text{me}} + \{\text{differential attenuation correction terms}\}$  where the differential attenuation is expressed in terms of the  $N_0(r)$  and  $D_0(r)$  at prior or subsequent ranges. In the initial-value form, the attenuation correction begins at the gate closest to the radar and proceeds outward. In the final value form, the correction terms are subtracted from the PIA so that the attenuation to range  $r$  is given as the path attenuation  $[0, r_n]$  minus the attenuation in the interval  $[r, r_n]$ .

[14] The equations can be solved numerically either by using a trapezoidal [Press *et al.*, 1992] or rectangular rule for the integrals; for the results presented a rectangular approximation is used. The final value formulation reduces to an iteration starting at the final range gate proceeding back toward the radar whereas the initial-value solution is found by iterating outward from the first gate. It should be noted, however, that the solution to (11a) or (12a) yields  $\delta I_b[f, D_0(r)] = \delta Z_c[f, D_0(r)]$  rather than the desired  $D_0(r)$ . To obtain  $D_0$  from  $\delta Z_c$  requires use of curves of the type shown in Figures 1 and 2. Once  $D_0$  is estimated,  $N_0$  can be found from (11b) or (12b).

[15] We use a simple simulation to check the performance of the above equations for several pairs of radar frequencies. Starting with 30-second averaged drop size distributions from an impact disdrometer, we fit to each distribution a gamma function with a best fit value of  $\mu$ . A temporal sequence of 32 such drop size distributions is then used to represent a particular range profile of the true raindrop size distributions for a 4 km path consisting of 32 range gates each of 0.125 km. Using these sets of raindrop size distributions, the measured reflectivity factors,  $Z_{\text{me}}(r_i)$ ,  $i = 1, \dots, 32$  for various pairs of frequencies are generated using (2) and (6)–(8). The  $Z_{\text{me}}(r_i)$  are next randomized using the fact that  $10 \log_{10} Z_{\text{me}}(r_i)$  is approximately normal with a mean equal to the true value and a standard deviation equal to  $5.57/\sqrt{n}$  (dB) (logarithmic detection), where  $n$  is the number of independent radar samples [Marshall and Hitschfeld, 1953]. In the retrieval we assume that  $\mu$  is fixed at 6 and that the upper branch of the  $D_0(r) - \delta Z_c$  solution is chosen. Although there are several ways to estimate the quantities  $\delta A_n(f)$  and  $A_n(f_1)$  in the final-value solution, (which include the surface reference technique as well as a radiometer-derived PIA), we consider in this paper the standard dual-frequency method that estimates  $\delta A_n(f)$  by a difference of differences [Eccles and Mueller, 1971]:

$$\begin{aligned} 2 \delta A_n(f) &= [\text{dB}Z_m(f_1, r_1) - \text{dB}Z_m(f_1, r_n)] - [\text{dB}Z_m(f_2, r_1) \\ &- \text{dB}Z_m(f_2, r_n)] \end{aligned} \quad (15)$$

[16] Having obtained  $\delta A_n(f)$ ,  $A_n(f_1)$  is found by a linear regression  $A_n(f_1) = a + b \delta A_n(f)$  based on sets of measured drop size distributions. The two sources of error in the  $\delta A_n(f)$  estimate given by (15) arise from the variability in the individual quantities because of the finite number of samples and from non-Rayleigh scattering effects. This second source of error can be understood by noting that in the absence of sampling errors, (15) can be written as  $2 \delta A_n(f) = [2 \delta A_n(f)]_{\text{true}} - E$  where the error term,  $E$ , is equal to  $[\text{dB}Z_c(f_1, r_1) - \text{dB}Z_c(f_1, r_n)] - [\text{dB}Z_c(f_2, r_1) - \text{dB}Z_c(f_2, r_n)]$ . This error is zero if the scatterers are Rayleigh at both frequencies and

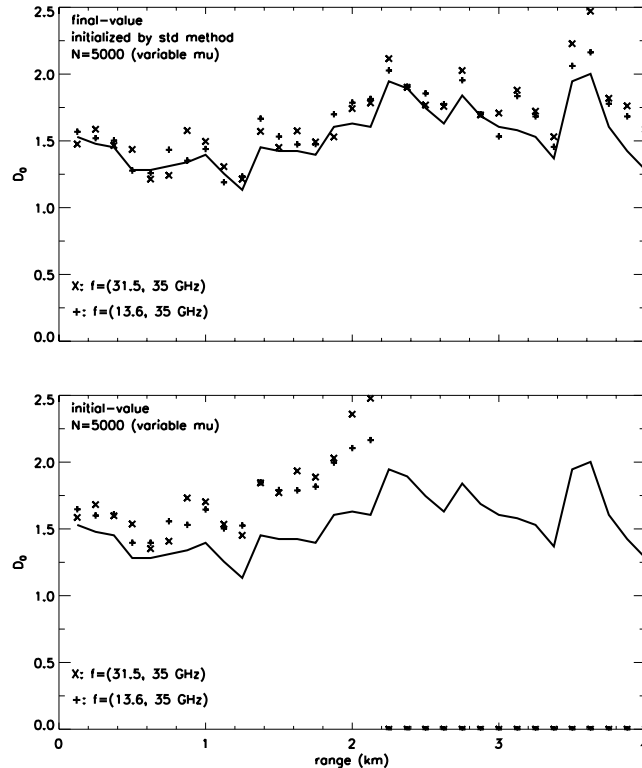


**Figure 8.** Retrievals of  $D_0$  from simulated radar data generated for the frequency pairs (13.6, 35 GHz) (+) and (31.5, 35 GHz) (X). The true  $D_0$  profile is given by the solid lines. Top: final-value solution; bottom: initial value solution.

at both ranges. However, since the basic method itself relies on non-Rayleigh scattering the error is generally nonzero for the frequencies of interest. Nevertheless, for the 4-km path selected in the simulation, the differential path attenuation is usually much larger than the non-Rayleigh scattering component and the estimate given by (15) is often sufficiently accurate. It is important to note in addition that the solution to (12a) and (12b) is fairly robust so that modest errors in the final values usually do not lead to divergence.

[17] A detailed analysis of the solutions to (11a), (11b), (12a), and (12b) is beyond the scope of the paper. Our purpose here is to describe the general behavior of the results and illustrate typical features. Shown in Figure 8 is an example of a  $D_0$  estimation using the final-value equations (top) and initial-value equations (bottom). Corresponding plots of rain rate and number concentration,  $N_t$ , were generated but not shown. In each plot, the true range-profile of  $D_0$  is represented by the solid line while the estimates derived from the [31.5, 35 GHz] and [13.6, 35 GHz] frequency pairs are represented by the “X” and “+” symbols, respectively. This example is typical in that the final-value solution is more stable than

the initial-value solution even when the quantities  $\delta A_n(f)$  and  $A_n(f)$  are not exact but determined by the procedure described above. In this particular example, the initial-value problem diverges in the sense that for the  $\delta Z_e$  obtained there is no corresponding solution of  $D_0$ . Also typical is the fact that the accuracy of the [31.5, 35 GHz] combination is comparable to that of the [13.6, 35 GHz] pair. This is the case, however, only when the number of independent samples,  $n$ , is greater than about 2000. For  $n < 1000$  the [31.5, 35 GHz] data yield  $D_0$  estimates that often exhibit large errors. Moreover, the solution often diverges for both the final-value and initial-value equations. Divergence in the solution becomes more common as the errors in  $\delta A_n(f)$  and  $A_n(f_1)$  increase and when the difference increases between the assumed value of  $\mu$  (=6) and the best fit values of  $\mu$  used in the true DSD profile.

[18] A second example of a  $D_0$ -retrieval is shown in Figure 9. For this case, we take the number of independent samples to be infinite, the  $\mu$  value to be equal to the true value, and the final values for the PIA to be exact. The only remaining error source, apart from the approximations used in transforming the integral equation to a matrix equation, is the ambiguity in estimating  $D_0$  from

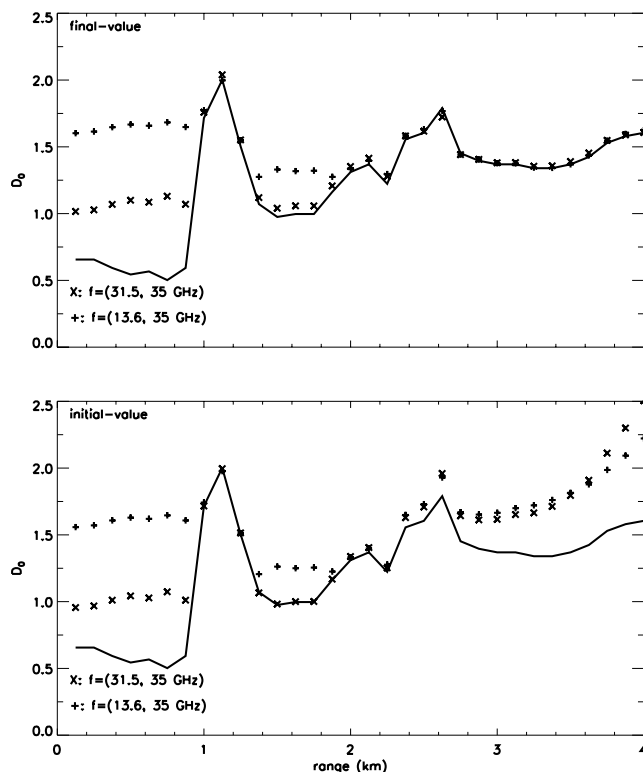


**Figure 9.** Same notation as in Figure 8 for a different  $D_0$  input profile. All errors except the  $D_0$ - $\delta Z_e$  ambiguity error have been set to zero.

$\delta Z_e$ . Since the upper branch of the solution is always selected, an error occurs if  $D_0$  falls below about 1.1 mm ( $\mu = 6$ ) in the case of the [13.6, 35 GHz] pair and below about 0.8 mm ( $\mu = 6$ ) in the case of the [31.5, 35 GHz] pair. For example, in the range from about 1.2 to 1.8 km the [31.5, 35 GHz] radar data can be used to recover accurate estimates of  $D_0$  while the [13.6, 35 GHz] data lead to overestimation. Over the first kilometer of the path, where  $D_0$  is less than 0.7 mm, both pairs of radar data yield large overestimates of  $D_0$ . This ambiguity can be resolved to some extent by using  $Z_e$  along with  $\delta Z_e$ . In particular, numerical calculations with measured drop size distributions suggest that the upper branch of the  $D_0$ - $\delta Z_e$ [13.6, 35 GHz] curve should be used if  $Z_e(13.6 \text{ GHz}) > 17 \text{ dB}$  and conversely. Similar considerations apply to the [31.5, 35 GHz] combination.

## 5. Summary and Conclusions

[19] By the use of a broadband antenna and power amplifier, it is possible to measure differential-frequency data using a radar that is not much larger or more complex than its single-frequency counterpart. Theoretical calculations indicate that differential Doppler and differential reflectivity data can be measured if a sufficient number of

independent samples can be collected. Frequencies at Ka-band with a separation on the order of 7% to 10% are attractive in that a modest antenna size (less than 1 m diameter) from low-Earth orbit can achieve a TRMM-type resolution of 4 km at the surface. Moreover, at these frequencies, the differential signals are relatively strong and closely related to the median mass diameter of the particle size distributions. Data measured at 9.1 GHz and 10 GHz by the EDOP radar in a zenith-viewing mode suggest that the differential velocity and reflectivity signals can be measured even at X-band frequencies and that the  $\delta Z_e$  (and to a lesser extent the  $\delta v$ ) signature is closely related to characteristics of the drop size distribution. While this is encouraging, it remains to be shown that the differential-frequency approach can estimate accurately the drop size distribution. To investigate this question, integral equations for the solution of the DSD parameters were presented in initial- and final-value forms. Simulated radar data from the [13.6, 35 GHz] and [31.5, 35 GHz] frequency pairs lead to reasonably good retrievals of  $D_0$  if the final-value forms of the equations are used. A partial resolution of the ambiguities in  $\mu$  and in the retrieval of  $D_0$  from  $\delta Z_e$  appears possible with some refinements in the algorithm. The greatest drawback of the differential reflectivity approach is the

need for large numbers of independent samples: simulations indicate unacceptably high errors in the estimates when this number falls below about 1000. Pulse compression, frequency agility and “whitening” [Koivunen and Kostinski, 1999] methods can be used to increase the number of independent samples. Nevertheless, the differential-frequency mode for airborne or spaceborne weather radar is best suited to nonscanning applications where there is usually sufficient time to acquire large numbers of samples.

## References

- Atlas, D., Advances in radar meteorology in *Advances in Geophysics*, vol. 10, pp. 318–478, Academic, San Diego, Calif., 1964.
- Bidwell, S. W., R. Meneghini, L. Liao, R. F. Rincon, and G. M. Heymsfield, Application of a differential reflectivity technique to the EDOP radar in ground-based operation, paper presented at IGARSS 2000, Honolulu, HI, pp. 1789–1791, Inst. of Electr. and Electron. Eng., New York, 2000.
- Doviak, R. J., and D. S. Zrnic, *Doppler Radar and Weather Observations*, 2nd edn., Academic, San Diego, Calif., 1993.
- Eccles, P. J., and E. A. Mueller, X-band attenuation and liquid water content estimation by dual-wavelength radar, *J. Appl. Meteorol.*, 10, 1252–1259, 1971.
- Heymsfield, G. M., et al., The EDOP radar system on the high-altitude NASA ER-2 aircraft, *J. Atmos. Oceanic Technol.*, 13, 795–809, 1996.
- Iguchi, T., and R. Meneghini, Differential equations for dual-frequency radar returns, *Prepr. 27th Conf. Radar Meteorol. Am. Meteorol. Soc.*, 190–193, 1995.
- Koivunen, A. C., and A. B. Kostinski, The feasibility of data whitening to improve performance of weather radar, *J. Appl. Meteorol.*, 38, 741–749, 1999.
- Kozu, T., et al., Development of precipitation radar onboard the Tropical Rain Measuring Mission (TRMM) Satellite, *IEEE Geosci. Remote Sens.*, 39, 102–116, 2001.
- Marshall, J. S., and W. Hirschfeld, Interpretation of the fluctuating echo from randomly distributed scatterers, 1, *Can. J. Phys.*, 31, 962–994, 1953.
- Matrosov, S. Y., Radar reflectivity in snowfall, *IEEE Trans. Geosci. Remote Sens.*, 30, 454–461, 1992.
- Meneghini, R., T. Kozu, H. Kumagai, and W. C. Bonczyk, A study of rain estimation methods from space using dual-wavelength radar measurements at near-nadir incidence over ocean, *J. Atmos. Oceanic Technol.*, 9, 364–382, 1992.
- Meneghini, R., L. Liao, S. W. Bidwell, and G. M. Heymsfield, On the feasibility of a Doppler weather radar for estimates of drop size distribution using two closely-spaced frequencies, *IEEE Trans. Geosci. Remote Sens.*, 39, 2203–2216, 2001.
- Press, W. H., S. A. Teukolsky, W. T. Vetterling, and B. P. Flannery, *Numerical Recipes in FORTRAN*, 2nd edn., 933 pp., Cambridge Univ. Press, New York, 1992.
- Ulbrich, C. W., Natural variations in the analytical form of the raindrop size distribution, *J. Clim. Appl. Meteorol.*, 22, 1764–1775, 1983.
- Zhang, G., J. Vivekanandan, and E. Brandes, A method of estimating rain rate and drop size distributions from polarimetric radar measurements, *IEEE Trans. Geosci. Remote Sens.*, 39, 830–841, 2001.

---

S. W. Bidwell, Code 556, NASA/Goddard Space Flight Center, Greenbelt, MD, USA.

G. M. Heymsfield, Code 912, NASA/Goddard Space Flight Center, Greenbelt, MD, USA.

L. Liao, Caelum Research Corp., Rockville, MD, USA.

R. Meneghini, Code 975, NASA/Goddard Space Flight Center, Greenbelt, MD, USA. (bob@priam.gsfc.nasa.gov)

R. Rincon, Code 555, NASA/Goddard Space Flight Center, Greenbelt, MD, USA.

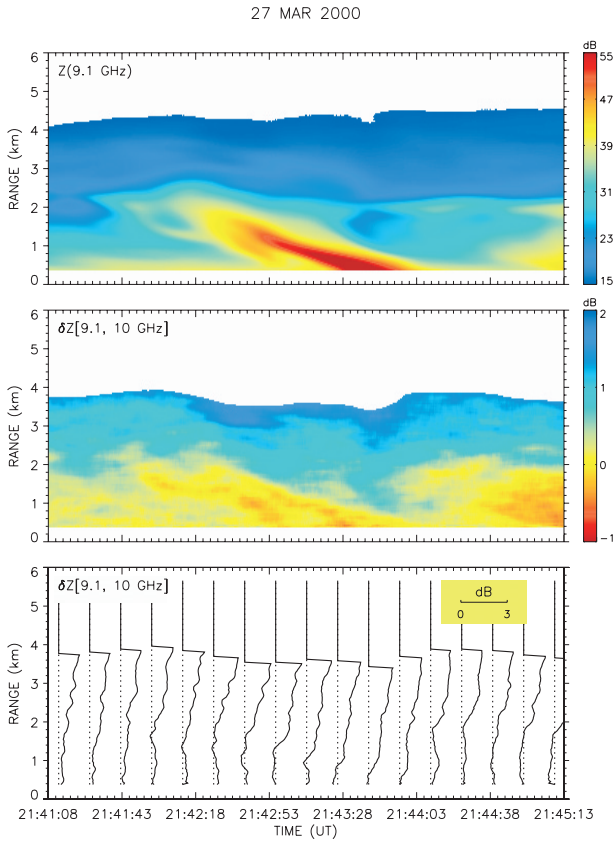


**Figure 4.** Height versus time plots of  $Z_{\text{mc}}(9.1 \text{ GHz})$  (top),  $\delta Z_{\text{mc}}[9.1, 10 \text{ GHz}]$  (center) and height profiles of  $\delta Z_{\text{mc}}[9.1, 10 \text{ GHz}]$  (bottom) over a 4 min segment of data.

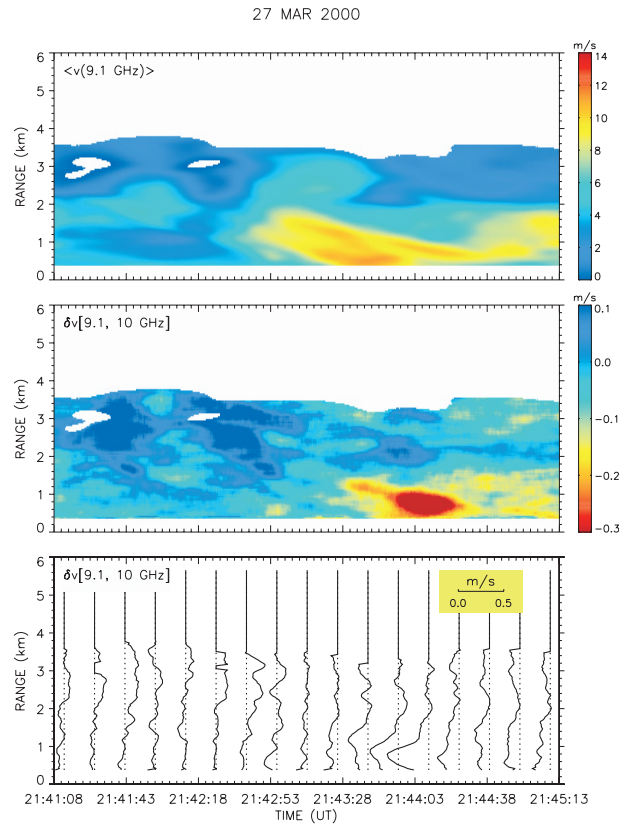


**Figure 5.** Height versus time plots of the mean Doppler velocity,  $\langle v(9.1 \text{ GHz}) \rangle$  (top),  $\delta v[9.1, 10 \text{ GHz}]$  (center) and height profiles of  $\delta v[9.1, 10 \text{ GHz}]$  (bottom) over same 4 min segment of data as in Figure 4.